

www.acsami.org Research Article

# Bottlebrush Thermoplastic Elastomers as Hot-Melt Pressure-Sensitive Adhesives

Mitchell R. Maw, Alexander K. Tanas, Erfan Dashtimoghadam, Evgeniia A. Nikitina, Dimitri A. Ivanov, Andrey V. Dobrynin, Mohammad Vatankhah-Varnosfaderani,\* and Sergei S. Sheiko\*



Cite This: https://doi.org/10.1021/acsami.3c07821



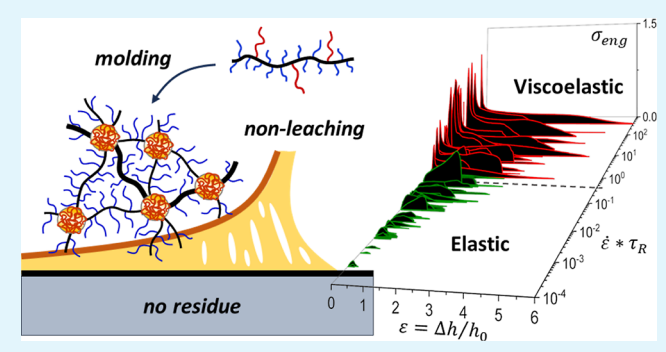
**ACCESS** I

III Metrics & More

Article Recommendations

s Supporting Information

ABSTRACT: Hot-melt pressure-sensitive adhesives (HMPSAs) are used in applications from office supplies to biomedical adhesives. The major component in HMPSA formulations is thermoplastic elastomers, such as styrene-based block copolymers, that provide both mechanical integrity and moldability. Since neat polymer networks are unable to establish an adhesive bond, large quantities of plasticizers and tackifiers are added. These additives enhance the adhesive performance but complicate the phase behavior and property stability of the pressure-sensitive adhesive. Herein, we introduce an alternative additive-free approach to HMPSA design based on self-assembly of bottlebrush graft-copolymers, where side chains behave as softness, strength, and



viscoelasticity mediators. These systems maintain moldability of conventional thermoplastic elastomers, while architecturally disentangled bottlebrush network strands empower several benefits such as extreme softness for substrate wetting, low melt viscosity for molding and 3D-printing, and a broad frequency range of viscoelastic responses for adhesion regulation within almost four orders of magnitude. The brush graft-copolymers implement five independently controlled architectural parameters to regulate the Rouse time, work of adhesion, and debonding mechanisms.

KEYWORDS: pressure-sensitive adhesives, thermoplastic elastomers, bottlebrush copolymers, polymer networks, mechanical properties

## ■ INTRODUCTION

Pressure-sensitive adhesives (PSAs) are mechanically distinct materials broadly used as high-performance tapes, transdermal drug delivery systems (TDDS), and soft robotics. ^1-5 A typical PSA is derived from a linear olefin, acrylate, or silicone network that can be either covalently or physically crosslinked. ^6-8 Physical networks, such as thermoplastic elastomers of styrenic block copolymers (SBCs), are vital in so-called hot-melt pressure-sensitive adhesives (HMPSAs) as they permit processing and fabrication in the melt state. <sup>9-11</sup> Single-component SBC networks exhibit fluidity at moderate temperatures (~100 °C), however, their viscoelastic behavior does not satisfy requirements for pressure-sensitive adhesion.

A primary condition for pressure-sensitive adhesion is establishing a large contact area to maximize the number of molecular interactions with a substrate. For an elastic material to spontaneously wet a substrate with a roughness of  $\sim 1~\mu m$ , the equilibrium modulus of the material should be below the Dahlquist criterion as  $G < G_C = 0.1~\mathrm{MPa.}^{12}$  Typical PSAs have a modulus within a range from  $10^3$  to  $10^5~\mathrm{Pa.}^6$  Such low modulus values are difficult to achieve in conventional linear polymer systems due to chain entanglements that set a lower limit of  $G > G_e$ , where the entanglement plateau modulus ranges from  $G_e \cong 0.1~\mathrm{MPa.}^{13}$  Along with softness for bonding, an

adhesive material should be stiff during debonding to transmit the bulk pull-off strain to the adhesive bonds at the interface, thus maximizing the local strain rate and tack stress. Stiffness also helps to prevent cohesive rupture of the PSA upon removal. The softness—stiffness dualism is met by configuring a particular viscoelastic response such that a soft PSA material exhibits an increase in modulus with frequency and maintains a high damping factor of tan  $\delta \sim 1.^{14-16}$  This enables the material to be soft enough to contour the substrate surface at a low bonding rate, stiff to enhance tack stress at higher debonding rates, and dissipative to increase the work of adhesion during debonding.  $^{17-20}$ 

The prescribed viscoelastic response for HMPSAs is difficult to achieve in conventional linear polymer systems due to inherent chain entanglements that (i) set a lower limit for the modulus as  $G > G_{\rm e} \cong \rho RT/(M_0 n_{\rm e})$  and (ii) confine the Rouse time to  $\tau_{\rm R} < \tau_0 n_{\rm e}^2$ , where  $\rho$  is the mass density,  $M_0$  is the molar

Received: May 31, 2023 Accepted: August 7, 2023



**ACS Applied Materials & Interfaces** 

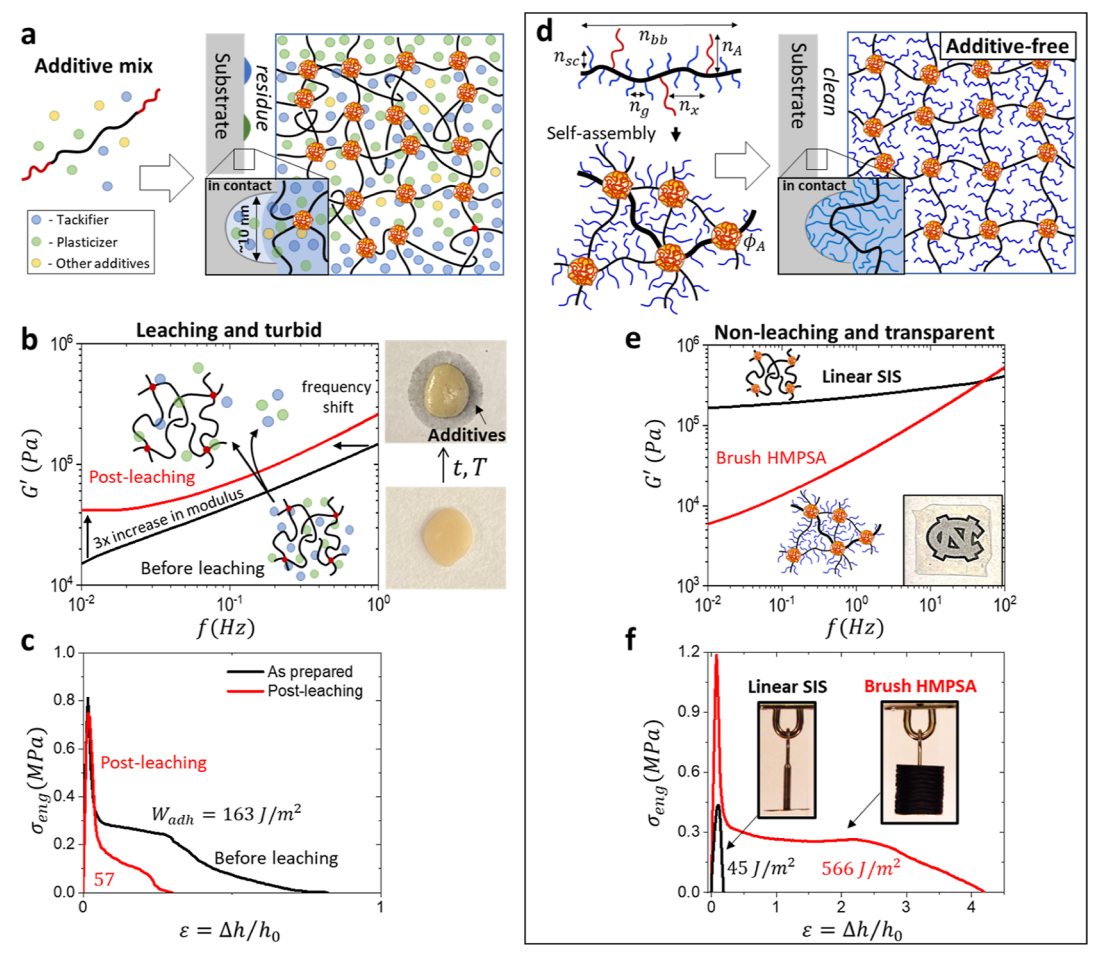


Figure 1. (a) Linear triblock copolymers require large quantities of plasticizers and tackifiers to attain the softness capable of wetting the surface of a substrate, which results in leftover residue upon debonding. (b) Storage modulus as a function frequency of a commercial ostomy adhesive reveals property variation as additives leach at 60 °C over a week. (c) Adhesive stress ( $\sigma_{\rm eng}$ ) as a function of pull-off strain (ε) for the commercial HMPSA from panel b reveals a three-fold decrease in the work of adhesion ( $W_{\rm adh}$ ). (d) A-g-B brush graft-copolymers instill additive-free structural control of viscoelasticity through the A-g-B architectural parameters, including the DPs of side chains ( $n_{\rm sc}$ ), of backbone spacers between neighboring side chains ( $n_{\rm g}$ ), between A-blocks ( $n_{\rm x}$ ), of the A-block  $n_{\rm A}$ , of the total brush strand  $n_{\rm bb}$ , and the volume fraction of the A-block  $\phi_{\rm A}$ . Side chains facilitate nanoscale wetting (inset) and intrinsically dilute the network backbone to expand viscoelastic properties. (e) Frequency sweep of the storage modulus in the PSA frequency window of commercial SIS and an exemplary brush HMPSA with architectural parameters  $n_{\rm sc} = 18$ ,  $n_{\rm g} = 1$ ,  $n_{\rm A} = 96$ ,  $\phi_{\rm A} = 0.05$ ,  $n_{\rm x} = 180$ , and  $n_{\rm bb} = 2000$ . While SIS is confined above the Dahlquist criterion, A-g-B brush graft-copolymers enable the ability to reach a modulus below 0.01 MPa at bonding frequencies by expanding the Rouse relaxation range. Inset: a 1 mm thick A-g-B film laid over a UNC logo demonstrates optical transparency of the material. (f) Adhesive stress as a function of pull-off strain for the materials from panel e displays a dramatic increase in adhesive performance. The A-g-B graft copolymer empowers over a 10× increase in  $W_{\rm adh}$ , calculated as  $W_{\rm adh} = h_0 \int_0^{e_{\rm max}} \sigma_{\rm eng}(\varepsilon) d\varepsilon$  compared to commercial SIS. The bond formed by linear SIS fails with the weight of the load-free hanging apparatus, while the brush HMPSA is able to upho

mass of a monomeric unit,  $n_e \cong 100$  is a typical entanglement degree of polymerization (DP), and  $\tau_0$  is the characteristic relaxation time defined by repeat unit chemistry. 21 To overcome these barriers, large quantities (~50 wt %) of plasticizer and tackifier are loaded into linear thermoplastic elastomers (Figure 1a). Both types of additives dilute chain entanglements to lower the G<sub>e</sub> below the Dahlquist criterion while concurrently imposing frequency shifts on the relaxation modulus spectra. 9,22 Specifically, the plasticizer causes a high frequency shift and the tackifier compensates for this shift by inducing the opposite effect to obtain the desired viscoelastic profile in the PSA frequency range. The resulting blends are prone to chemical migration, resulting in property variation over time, interfacial leaching, and residue left on substrates after debonding (Figure 1b,c).<sup>23-27</sup> In addition, multicomponent systems suffer from selective miscibility of the constituting polymer blocks and additives. 28,29 For example, SIS-based adhesives may become

opaque due to temperature-dependent segregation of terpene, petroleum, or rosin tackifiers.<sup>30</sup> Moreover, the abundance of commercial HMPSA formulations convolutes structure—property correlations, making design and property control of adhesive materials a trial-and-error process.

To remedy the inherent drawbacks of mixture-based HMPSAs, we develop an alternative, additive-free approach by implementing the viscoelastic demands of moldable PSAs into a single-molecule system via A-g-B bottlebrush graft-copolymers, where a controlled fraction of linear A-blocks is dispersed along a bottlebrush B-block (Figure 1d). The polymer network is formed by self-assembly of the A-g-B macromolecules due to microphase separation of the chemically and architecturally dissimilar blocks such that the glassy domains of linear A blocks play the role of network nodes, while the bottlebrush network strands regulate the viscoelastic response. The lack of macrophase separation in the single-component A-g-B materials allows

Table 1. Mechanical Properties and Rouse Time of Brush HMPSAs

$n_{\rm g}^{a}$	$n_{\rm sc}^{b}$	$n_{\rm x}^{\ c}$	$n_{\rm A}^{d}$	$\phi_{\scriptscriptstyle  m A}^{\;\;e}$	$n_{\rm bb}^{f}$	Gg (kPa)	$\beta^h$	$E_0^i$ (kPa)	$\lambda_{\max}^{j}$	$\sigma_{\max}^{k}$ (kPa)	$\tau_{R}(s)^{l}$
				PS	-g-PIB $(n_g = 1)$	), Longer Backbo	one $(n_{bb} = 20)$	000)			
1	18	180	96	0.047	2000	1.8	0.54	18.1	2.6	267	83.0
1	18	180	278	0.126	2000	2.7	0.70	61.8	2.0	479	7.6
1	18	180	414	0.177	2000	2.9	0.72	76.1	1.9	480	4.1
1	18	180	504	0.208	2000	3.4	0.74	104	2.3	1383	1.6
				PS	$S$ - $g$ -PIB ( $n_g = 1$	1), Shorter Backb	one $(n_{bb} = 9)$	900)			
1	18	163	54	0.030	900	1.7	0.56	19.3	2.0	46	95.6
1	18	163	76	0.042	900	1.8	0.59	23.3	2.0	98	46.0
1	18	163	125	0.067	900	3.2	0.68	66.5	1.8	216	10.2
1	18	163	468	0.212	900	3.4	0.80	176	1.6	427	3.3
					PS-g-P	IB $(n_g = 8)$ , $n_x Va$	riation				
8	18	218	60	0.106	938	44.3	0.23	193	3.5	2040	0.83
8	18	332	60	0.075	1237	32.4	0.17	127	3.9	1540	3.4
8	18	503	60	0.048	1265	15.6	0.16	59.9	3.9	740	12.5
8	18	906	60	0.030	805	2.6	0.03	8.00	5.3	110	600
					PS-g-Pl	IB $(n_{\rm g} = 8)$ , $n_{\rm sc}  {\rm Va}$	ariation				
8	18	216	60	0.108	1319	56.7	0.20	232	4.7	3520	0.83
8	23	165	60	0.10	764	36.3	0.21	154	2.9	1030	1.8
8	41	135	60	0.10	465	8.7	0.25	39.3	3.09	410	15.6
					PS-g-PIB (ng	= 8), Longer A B	$lock n_A = 12$	0			
8	18	450	120	0.10	854	24.3	0.24	94.9	3.84	1560	2.5
8	18	803	120	0.05	NA	6.7	0.16	25.6	4.75	980	26.9
					1	$PS-g-PIB (n_g = 4)$	)				
4	18	149	60	0.10	1134	28.2	0.37	171	2.88	1820	0.8
4	18	360	60	0.05	1259	11.9	0.22	51.0	3.63	790	4.1
4	41	112	60	0.10	251	9.9	0.47	79.6	2.19	370	3.98

<sup>a</sup>Grafting density of side chains on the backbone with the BA spacer. <sup>b</sup>DP of PIB side chains in the B-block. <sup>c</sup>Numerical average DP of the brush backbone between glassy block side chains that physically crosslink. <sup>d</sup>Numerical average DP of each glassy block side chain as determined by <sup>1</sup>H NMR. <sup>e</sup>Volume fraction of the glassy block, calculated using the following density values:  $\rho_{\text{PIB}} = 0.92 \text{ g/mL}$ ,  $\rho_{\text{PS}} = 1.02 \text{ g/mL}$ ,  $\rho_{\text{PEG}} = 0.94 \text{ g/mL}$ , and  $\rho_{\text{PBA}} = 1.08 \text{ g/mL}$ . <sup>f</sup>Numerical average DP of the total brush strand. <sup>g</sup>Structural shear modulus. <sup>h</sup>Strain-stiffening parameters are fitting parameters in eq S1. <sup>i</sup>Apparent Young's modulus which can be determined either as a tangent of a stress–strain curve at  $\lambda \to 1$  or be calculated from eq S2. <sup>j</sup>Maximum elongation at the sample rupture. <sup>k</sup>Maximum stress-at-break (strength) of brush HMPSAs. <sup>l</sup>Experimentally determined Rouse time of brush HMPSAs from Figures S35–S37.

Scheme 1. Synthesis of (a) PS-g-PIB ( $n_g = 1$ ) and (b) PS-g-PIB ( $n_g > 1$ ) Brush Graft-Copolymers for HMPSAs with Chain Transfer Agents and Initiator End Groups Omitted (See Supporting Information for Full Synthetic Details)

a Br 
$$n_{sc}$$
 RAFT  $n_{sc}$   $n_{sc}$  ATRP  $n_{sc}$   $n_{sc}$   $n_{sc}$   $n_{sc}$   $n_{sc}$   $n_{sc}$   $n_{sc}$   $n_{sc}$   $n_{sc}$   $n_{bb}$   $n_{a}$   $n_{bb}$   $n_{b}$   $n_{b}$ 

**ACS Applied Materials & Interfaces** 

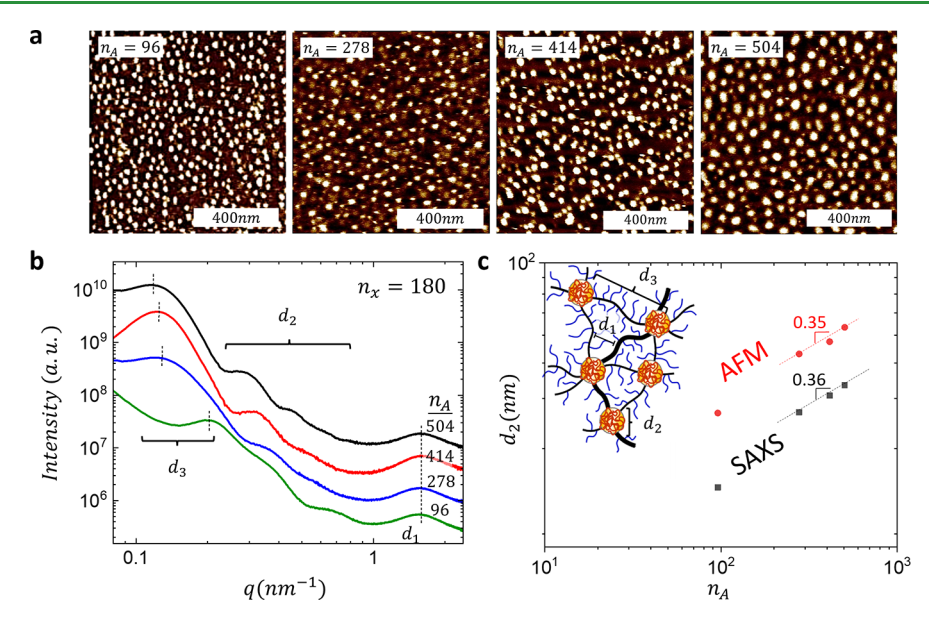


Figure 2. (a) AFM and (b) SAXS of PS-g-PIB ( $n_{\rm g}=1$ ) samples with identical B-blocks ( $n_{\rm sc}=18$ ,  $n_{\rm g}=1$ ,  $n_{\rm x}=180$ , and  $n_{\rm bb}=2000$ ) and variable  $n_{\rm A}$  as indicated. The AFM micrographs display a granular structure ascribed to microphase separation of PS A-domains uniformly dispersed in the bottlebrush matrix of PIB B-blocks. Both the domain size and interdomain distance increase with  $n_{\rm A}$ . (b) SAXS curves verify the brush topology of PS-g-PIB ( $n_{\rm g}=1$ ) samples with variable  $n_{\rm A}$ . The interbrush distance ( $d_1$ ), A-domain diameter ( $d_2$ ), and interdomain distance ( $d_3$ ) of the networks corroborate results observed by AFM where the  $d_2$  and  $d_3$  peaks increase with  $n_{\rm A}$ , while the  $d_1$  peak remains constant (Table 2). (c) A-domain diameter ( $d_2$ ) scaling with  $n_{\rm A}$  corroborated by AFM and SAXS. The  $d_2$  from AFM was calculated as a mean of >100 protruding domains from the height profiles for each sample (Figure S22). Both methodologies show the increase in domain size as  $d_{\rm A} \sim n_{\rm A}^{0.35\pm0.08}$  by AFM and  $d_{\rm A} \sim n_{\rm A}^{0.36\pm0.02}$  by SAXS. Exaggerated  $d_2$  from AFM is a result of convolution with the tip shape.

the preparation of optically transparent films (Figure 1e, inset) depending on side chain length ( $\sim n_{\rm sc}$ ) and grafting density  $(\sim n_{\rm g}^{-1})$ , and the entanglement DP may increase up to  $n_{\rm e} \cong 2000$ , which effectively disentangles the network strands, allowing the softness of  $G \sim 10^3$  Pa (Table 1).<sup>31,32</sup> The disentanglement of network strands expands the Rouse relaxation regime as  $\tau_{\rm R} = \tau_0 n_{\rm sc} (n_{\rm x}/n_{\rm g})^2$  to allow the brush PSA to satisfy the Dahlquist criterion by reducing the modulus at bonding frequencies (Figure 1e), while side chains exhibit limited entropic penalty to wet nanoscale pores (Figure 1d, inset).<sup>33</sup> In addition, steric repulsion between densely grafted side chains extends the backbone into the finite extensibility range, resulting in modulus increase with deformation, which prevents cohesive rupture of soft HMPSAs. The strain-stiffening behavior is quantified by the parameter  $\beta \equiv \langle R_{\rm in}^2 \rangle / R_{\rm max}^2$  which describes the ratio of the mean square end-to-end distance to the square of the contour length of a network strand.<sup>34</sup> Additional strength enhancement is provided by mesh interconnectivity in A-g-B networks given multiple A-blocks per network strand.<sup>35</sup> The combination of the intrinsic softness, firmness, and interfacial wetting results in a dramatic enhancement of the adhesive performance for brush HMPSAs (Figure 1f). It is important to emphasize that the architectural control over thermomechanical properties is performed without using additives, which allows the formulation of HMPSA materials for a wide range of applications without the detrimental effects of uncontrolled leaching and phase transformations.

## ■ RESULTS AND DISCUSSION

**Synthesis of Brush HMPSAs.** A comprehensive library of A-g-B bottlebrush graft-copolymers (Figure 1d) with parameters ranging around  $n_{\rm sc} = 18-41$ ,  $n_{\rm g} = 1-8$ ,  $n_{\rm A} = 60-504$ ,  $\phi_{\rm A} = 0.025-0.212$ ,  $n_{\rm x} = 135-906$ , and  $n_{\rm bb} = 400-2000$  was

synthesized to demonstrate the scope of architectural control over structural, thermodynamic, and viscoelastic properties (Table 1). Different polymerization techniques were used to prepare A-g-B brush graft-copolymers depending on the grafting density of the brush block (Scheme 1). Sequential reversible addition-fragmentation chain-transfer(RAFT) and atom transfer radical polymerization (ATRP) were utilized to synthesize densely grafted poly[MA-g-(PIB/PS)], hereto denoted as PS-g-PIB  $(n_g = 1)$ , where incorporation of styrene monomers aided solubility of brush blocks (Scheme 1a). For less dense backbones, one-step free-radical polymerization (FRP) of macromonomers was utilized to synthesize poly[nBA-ran-MAg-(PIB/PS)], hereto referred to as PS-g-PIB ( $n_g > 1$ ) (Scheme 1b). The architectural parameters of these A-g-B brush graftcopolymer networks  $n_{\rm sc}$ ,  $n_{\rm g}$ ,  $n_{\rm A}$ ,  $\phi_{\rm A}$ ,  $n_{\rm x}$ , and  $n_{\rm bb}$  were determined by combination of <sup>1</sup>H NMR and GPC (Figures S1-S21). Consumption of spacers and macromonomers was investigated by <sup>1</sup>H NMR, and subsequent analysis provided information on their distribution throughout the A-g-B brush graft-copolymer backbone. The PIB macromonomer appears to propagate faster than the BA spacer, resulting in gradient distribution (Figure S20). At 30% conversion, the average cumulative  $n_g = 4$  was measured and gradually converged to the target  $n_g = 8$  at higher conversions.

**Structural and Thermal Analysis.** The synthesized bottlebrush graft-copolymers undergo microphase separation of the linear PS and brush PIB blocks to form a robust physical network with PS domains acting as physical crosslinks. Atomic force microscopy (AFM) and small-angle X-ray scattering (SAXS) were performed to investigate the effect of different architectural parameters on network morphology. AFM imaging of A-g-Bs with identical  $n_{\rm sc}=18$ ,  $n_{\rm g}=1$ ,  $n_{\rm x}=180$ , and  $n_{\rm bb}=2000$  corroborated microphase separation, where the domain size increases from  $29.6\pm3.5$  to  $59.3\pm5.9$  nm with the DP of PS

from  $n_A$  = 96 to  $n_A$  = 504, respectively (Figures 2a, S22 and Table S2). Since AFM measurements are generally affected by various surface effects and convolution of the AFM tip shape, SAXS was employed to acquire more accurate information about network morphology including the interbrush distance ( $d_1$ ), A-domain diameter ( $d_2$ ), and interdomain distance ( $d_3$ ) (Figure 2b and Table 2). While  $d_1$  remains constant (as expected for the same B-

Table 2. Microphase-Separated Morphology of A-g-B Bottlebrush Graft-Copolymers ( $n_{sc} = 18$ ,  $n_g = 1$ ,  $n_x = 180$ , and  $n_{bb} = 2000$ ) from SAXS

$n_{\rm A}$	$\phi_{ ext{A}}$	$d_1^a$ (nm)	$d_2^a$ (nm)	$d_3^a$ (nm)	$RSD_2^b$	$d_3 - d_2  (\mathrm{nm})$
96	0.053	4.1	16.2	29.0	0.18	12.8
278	0.121	4.0	29.8	44.8	0.18	15.0
414	0.166	3.9	34.1	47.6	0.14	13.5
504	0.202	4.0	37.1	48.3	0.12	11.2

"The interbrush distance  $(d_1)$ , A-domain diameter  $(d_2)$ , and interdomain distance  $(d_3)$  (Figure 2c). Relative standard deviation of the domain diameter.

block), the domain diameter increases with  $n_{\rm A}$ , showing a good agreement with the theoretical dependence  $d_2\cong (n_{\rm bb}n_{\rm A}\nu_{\rm A})^{1/3}$  for microphase-separated brush networks (Figure 2c). <sup>36</sup> The corresponding increase in the interdomain distance (distance between A-domain centers) is largely due to the  $d_2$  contribution, while the distance between the domain interfaces  $d_3-d_2$  is nearly identical for samples with the same  $n_{\rm x}$  (Table 2). Along with the  $n_{\rm A}$  effect, variations in  $n_{\rm sc}$ ,  $n_{\rm g}$ , and  $n_{\rm x}$  provide additional architectural levers to vary interbrush distance and interdomain distance (Figures S23–S26).

A primary trait of HMPSAs is the ability to flow at moderate temperatures to reduce the risk of polymer degradation during processing and fabrication. The onset of flow  $(T_{\rm flow})$  is identified as the temperature where the loss modulus (G') surpasses the storage modulus (G') of the material during oscillatory shear measurements (Figure S34). The effect of A-g-B architecture on  $T_{\rm flow}$  is exemplified by two series of PS-g-PIB samples with systematically varied volume fractions of the PS A-block  $(\phi_{\rm A})$ . In the first series PS-g-PIB  $(n_{\rm g}=1)$ ,  $\phi_{\rm A}$  was varied from 0.03 to 0.07 by increasing  $n_{\rm A}$  from 54 to 125 at constant

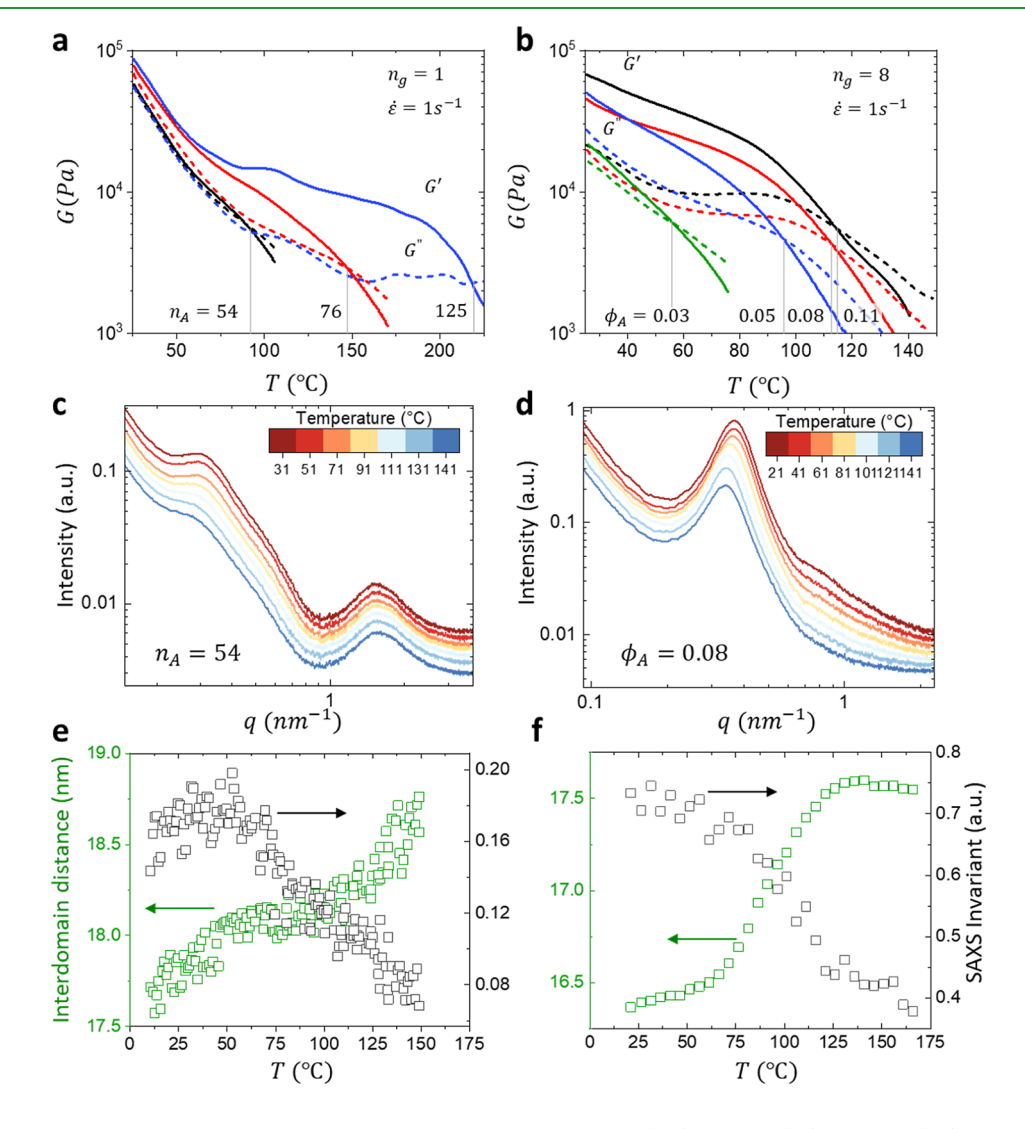


**Figure 3.** Brush HMPSAs melt at moderate temperatures dependent on  $n_A$  and  $\phi_A$ . (a,b) Storage (G') and loss (G'') moduli as a function of temperature for (a) brush ( $n_g = 1$ ) and (b) comb ( $n_g = 8$ ) HMPSAs with  $n_{sc} = 18$  and variable  $n_A$  as indicated. (c,d) SAXS spectra for the sample with (c)  $n_A = 54$ ,  $n_g = 1$  and (d)  $\phi_A = 0.08$ ,  $n_g = 8$  from panels a and b at different temperatures. (e,f) The interdomain distance  $d_3$  peak (Figure 2c) shifts to lower q and the SAXS invariant decreases, indicating domain dissociation.

dimensions of the B-block ( $n_{\rm sc}=18,\,n_{\rm x}=163$ ), which led to a  $T_{\rm flow}$  increase within  $T_{\rm flow}=91-218$  °C (Figure 3a). In the second series PS-g-PIB ( $n_{\rm g}=8$ ),  $\phi_{\rm A}$  was varied from 0.03 to 0.10 by decreasing  $n_{\rm x}$  from 906 to 216 at a constant  $n_{\rm A}=60$ , to show a relatively low  $T_{\rm flow}$  increasing from 56 to 114 °C, respectively (Figure 3b). Disassembly of physical crosslinks at the onset of flow was corroborated by SAXS measurements during heating (Figure 3c,d) by monitoring the interdomain distance ( $d_{\rm 3}$ ) and SAXS invariant (Figure 3e,f). The invariant decrease is caused by a decrease in both the volume fraction of the minority PS phase and the electron density contrast due to PS/PIB mixing at elevated temperatures. The observed  $T_{\rm flow}$  increase is consistent with the increase in  $\phi_{\rm A}$  and total DP of A-g-B macromolecules N established for linear block copolymers (Table 3).  $^{38,39}$  However,

Table 3. Flow Temperature of A-g-B Brush-Like Graft-Copolymers with Different Architectures

$n_g^a$	$n_{\rm sc}^{a}$	$n_{\rm x}^{a}$	$n_{\rm A}^{a}$	$\phi_{\text{A}}^{}a}$	$n_{\rm bb}^{a}$	$N = n_{\rm bb} (1 + n_{\rm A}/n_{\rm x})^b$	$T_{\text{flow}}$ (°C)		
Bottlebrush $(n_{\rm g} = 1)$									
1	18	163	54	0.03	900	1198	92		
1	18	163	72	0.04	900	1298	147		
1	18	163	125	0.07	900	1590	218		
Comb $(n_{\rm g} = 8)$									
8	18	906	60	0.03	805	858	56		
8	18	503	60	0.05	1265	1416	95		
8	18	332	60	0.08	1237	1461	112		
8	18	216	60	0.11	1319	1685	114		
a						1.			

"Architectural parameters as outlined in Table 1. "Total DP of the Ag-B scaffold. "Flow temperature identified as the temperature where the loss modulus (G'') surpasses the storage modulus (G') of the material during oscillatory shear measurements.

linear and brush HMPSAs differ in the effect of  $n_{\rm A}$  on mechanical properties. For example, increasing  $n_{\rm A}$  at a constant  $n_{\rm x}$  for linear SIS copolymers entails a corresponding shift in  $\phi_{\rm A}$ , yielding a stiff material with high  $T_{\rm flow}$ . When it comes to brush HMPSAs, however, high  $n_{\rm A}$  values can be reached at low  $\phi_{\rm A}$  by increasing the volume fraction of the brush block.

Controlling Adhesive Performance through Viscoe**lastic Response.** The effect of the brush motif  $(n_{sc}, n_g, \text{ and } n_x)$ on viscoelasticity has been reported previously for covalent bottlebrush networks, <sup>33</sup> where an increase in  $n_{\rm sc}/n_{\rm g}$  and  $n_{\rm x}$  led to systematic shifts in the Rouse time, defining a crossover from viscoelastic to elastic mechanical response. Here, we will consider the effect of the A-block. Brush HMPSA systems have both  $n_A$  and  $\phi_A$  as additional levers for tuning viscoelasticity. Frequency sweeps within the PSA frequency range for samples with  $n_A$  from 504 to 96 exhibit a decrease in G'with expansion of the Rouse relaxation regime before the onset of the elastic plateau (Figure 4a). The Rouse times of all samples were experimentally determined by uniaxial testing at various strain rates  $(10^{-4} \text{ to } 10^1 \text{ s}^{-1})$  (Figures S35 and S36). Correlations were derived by isolating the effect of  $n_A$  (and  $\phi_{\rm A}$ ) on the estimated Rouse time normalized by known architectural contributions from  $n_{sc}$ ,  $n_{gr}$  and  $n_{x}$  (Figures 4b and S37).<sup>33</sup> The observed  $n_{A}^{-1.7}$  power law is purely empirical and has no theoretical justification, which is encumbered by the chemical heterogeneity of A-g-B networks.

The ability to tune the HMPSA viscoelasticity by regulating polymer architecture enables further programming of the work of adhesion and debonding mechanisms. The work of adhesion  $(W_{adh})$  of the brush HMPSAs was measured by probe tack testing at strain rates ( $\dot{\varepsilon}$ ) from approximately 0.001–1 s<sup>-1</sup> and further normalized by the film thickness and elastic modulus (Figures 4a, S38 and S39).<sup>20</sup> It is important to recognize that  $W_{\text{adh}}$  spans almost four orders of magnitude without using additives for the range of parameters in this study. By offsetting the strain rate by the experimentally determined  $\tau_R$  of each prospective sample, all data points fall on a single line (Figure 4b). The brush HMPSA samples experience an apparent shift in scaling for the  $W_{\rm adh}$  and debonding mechanisms at  $\dot{\varepsilon} \cong \tau_{\rm R}^{-1}.^{33,41}$ The normalized work of adhesion scales as  $W_{\rm adh}/E_0 \sim \dot{\varepsilon} au_{
m R}$  while debonding at a rate below the Rouse rate  $(\tau_R^{-1})$ , which is dictated by cavity crack propagation along the surface of the substrate. Debonding above the Rouse rate is governed by cavity growth into the bulk followed by fibrillation, which scales as  $W_{\rm adh}/E_0 \sim (\dot{\varepsilon}\tau_{\rm R})^{1/2}.^{17,20}$  This is summarized in a plot of overlaid probe tack tests where the change in debonding mechanisms is observed at  $\dot{\varepsilon} \cong \tau_R^{-1}$  (Figure 4c). Viscoelastic debonding above  $\tau_{\rm R}^{-1}$  exhibits the characteristic tack peak  $(\sigma_{\text{max}})$  at small deformations as a result of the transition from bulk deformation to nucleation of cavities. By utilizing the correlation between architecture and relaxation dynamics, adhesive performance can be programmed from elastic to viscoelastic deformation in the absence of additives.

A unique feature of A-g-B brush architecture is the ability to regulate the deformation response at both small and large deformations. At small deformations specifically, we can tune the modulus and Rouse time to cover a broad-range work of adhesion spanning elastic to viscoelastic regimes (Figure 4d). At larger deformations, A-g-Bs demonstrate an intense strainstiffening behavior where the initially soft sample stiffens rapidly with deformation, which mimics that of biological tissues and prevents cohesive rupture of adhesives (Figures S27-S30).35 For example, the sample with  $n_{sc} = 18$ ,  $n_{g} = 1$ ,  $n_{A} = 504$ ,  $n_{x} = 180$ , and  $n_{\rm bb}$  = 2000 exhibits the characteristic J-shaped curve almost identical to a rtic tissue while maintaining a  $\sigma_{\rm tack}$  above 1 MPa and  $W_{\rm adh} \sim 100 \, {\rm J/m^2}$  (Figures 5a and S38).<sup>42</sup> Brush HMPSAs are capable of tuning the modulus, Rouse time, and strainstiffening independent of one another, which allows for the generation of very unusual (distinct) debonding profiles. For example, we compare samples with different combinations of the Rouse time and strain-stiffening parameter that are pulled off at a near identical debonding rate of  $\dot{\varepsilon} \sim 1 \text{ s}^{-1}$  (Figure 5b). The sample with  $\tau_R$  = 4.0 s undergoes the typical viscoelastic debonding  $(\tau_R \dot{\varepsilon} > 1)$  exhibited by a pronounced tack peak followed by an extended yielding plateau, which decays with deformation due to low strain-stiffening ( $\beta = 0.17$ ). In contrast, the sample with  $\tau_R = 0.8$  debonds elastically ( $\tau_R \dot{\varepsilon} < 1$ ) with no tack peak but a strong increase in pull-off stress with deformation due to more intense strain-stiffening ( $\beta$  = 0.37). A sample with intermediate values of  $\beta$  and  $\tau_R$  shows an intermediate debonding behavior, exhibiting both a weak tack peak and a limited strain-stiffening effect.

Brush HMPSAs also bolster their mechanical integrity with the ability to independently tune strength by architecture independent of modulus and strain-stiffening.<sup>35</sup> Brush networks with varying  $n_{\rm bb}$  were compared to isolate the effect of strength on adhesion. Two densely grafted samples with  $n_{\rm bb} = 900$  and  $n_{\rm bb} = 2000$  display near identical  $E_0$  and  $\beta$  but a 2-fold increase in cohesive strength (Figure S40). This yields a near-identical adhesion response at small deformations via probe tack test,

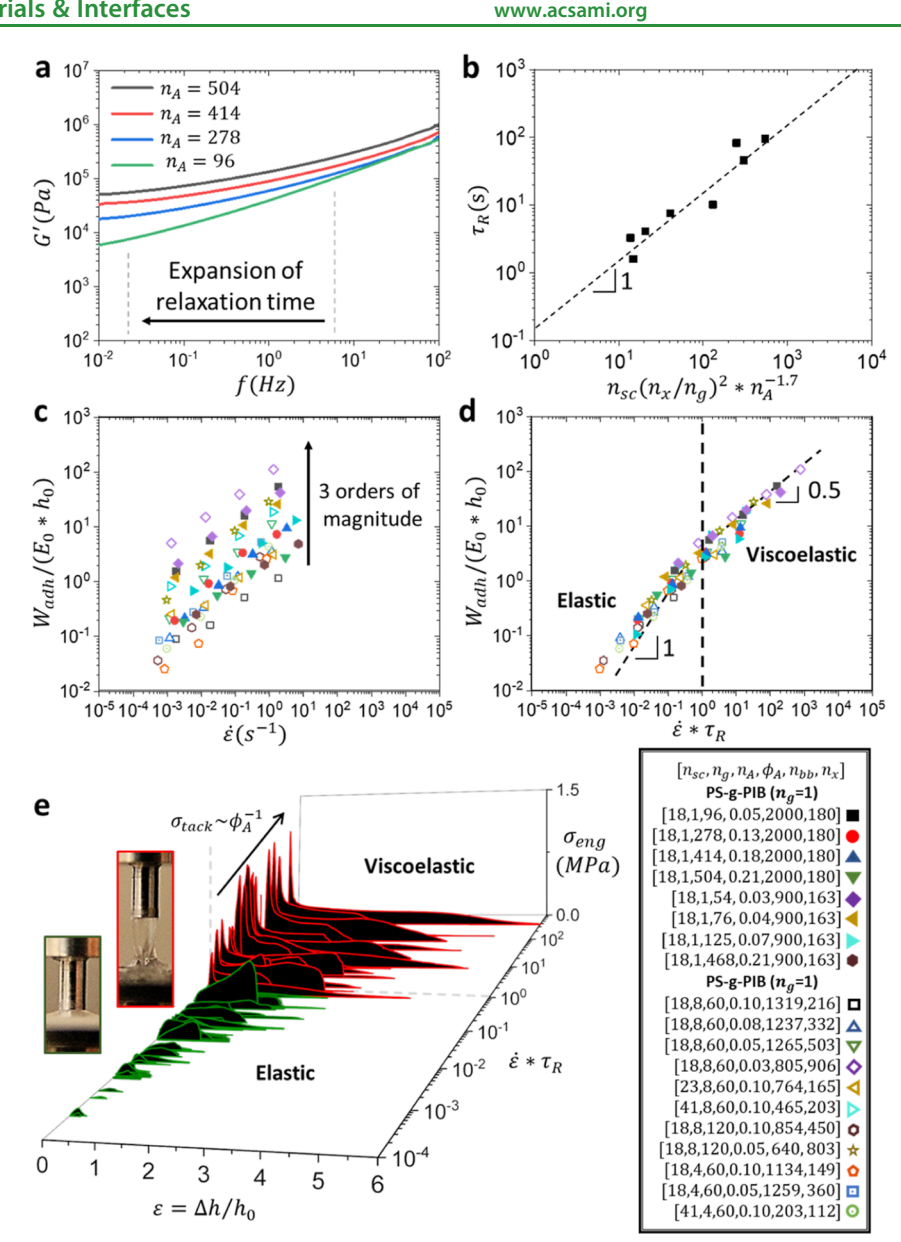
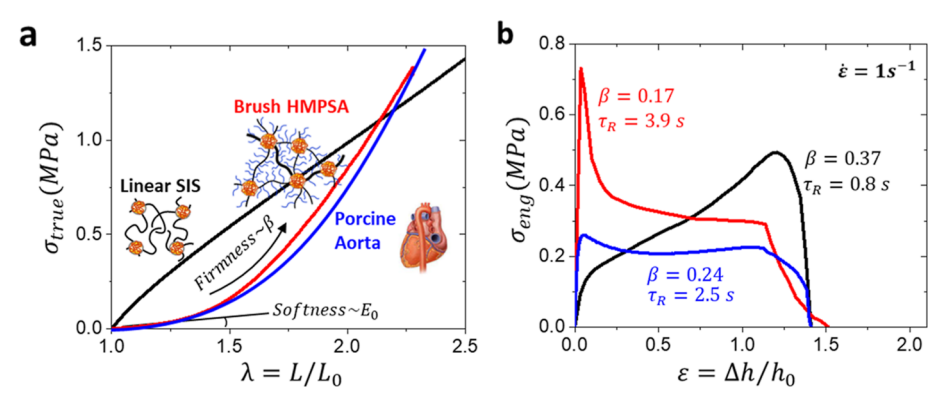


Figure 4. Additive-free brush HMPSAs architecturally tune adhesive performance. (a) Frequency sweeps of the storage modulus (G') in the PSA frequency window for PS-g-PIB ( $n_{\rm g}=1$ ) samples with varying  $n_{\rm A}$ . Decreasing  $n_{\rm A}$  produces an extension of time-dependent mechanical properties which lower the elastic plateau. (b) Rouse time ( $\tau_R$ ) scales with A-g-B brush architectural parameters. The  $\tau_R$  of the PS-g-PIB ( $n_e = 1$ ) samples scale with previously determined parameters of the brush strand<sup>33</sup> and an additional structural coefficient. (c) Normalized work of adhesion as a function of the strain rate for all brush HMPSA samples. The work of adhesion can be programmed over three orders of magnitude by tuning the macromolecular structure alone without the use of additives for samples in the legend on the lower right (Table 1). (d) All data points from c fall on a single line where a rate-dependent shift from elastic to viscoelastic debonding is revealed at  $\dot{\varepsilon} = \tau_{\rm R}^{-1}$ . (e) Overlaying probe tack test curves of all brush HMPSAs according to the normalized strain rate  $(\dot{\epsilon}\tau_R)$  reveals systematic control of debonding mechanisms. Debonding the probe below the Rouse rate  $(\tau_R^{-1})$  results in an elastic debonding mechanism where cavity growth is dominated by crack propagation in the plane of the interfacial bond. At higher rates, viscoelastic debonding occurs where interfacial cavities expand into the bulk and form fibrils with increased strain.

while the strength directly increases strain at the break  $(\varepsilon_{\text{max}})$  of cohesive fracture.

The architectural platform for the design of HMPSAs enables hot-melt processing of tapes with programmable viscoelasticity and melting temperature (Figure 6a). Small quantities of brush HMPSAs with varying  $\phi_A$  were pressed into a cellulose backing at 140 °C for a short time, resulting in a 10  $\mu$ m layer of adhesive. The films were cut and wound around a spool to produce brush HMPSA tapes with different adhesive performances. This is displayed in their ability to uphold various loads through zerodegree shear tests (Figure 6b). Additionally, the low viscosity of

the brush HMPSA at increased temperatures enables loading of active agents in biomedical adhesives like TDDSs (Figure 6c). For example, nicotine was added to the brush HMPSA at 120 °C and mixed until homogenously distributed. The sample may then be hot-melt pressed (like in Figure 6a) or 3D-printed into shapes that are more beneficial to flexibility on the skin of a patient. Nicotine may then diffuse through the skin of the patient like a commercial nicotine patch.



**Figure 5.** Control over debonding mechanisms and firmness. (a) Comparing stress—elongation curves of brush HMPSAs to those of linear networks and biological tissue. Intrinsically entangled linear SIS networks demonstrate a conventional stress—strain behavior characterized by a relatively high modulus above  $10^5$  Pa and stiffness decay with deformation (black curve). Architecturally disentangled brush HMPSAs demonstrate a lower modulus followed by intense stiffness increase with deformation (red curve), which mimics the softness and firmness of biological tissue (blue squares) displayed by the sample. (b) Independently controlling Rouse time ( $\tau_R$ ) and firmness (β) leads to distinct probe tack test profiles when being debonded at strain rates above or below their Rouse rate ( $\tau_R^{-1}$ ). The sample ( $n_{sc} = 18$ ,  $n_g = 8$ , and  $n_x = 332$ ) with  $\tau_R = 3.9$  s undergoes viscoelastic debonding ( $\tau_R\dot{\epsilon} > 1$ ) with a characteristic tack peak followed by a decaying yielding plateau (red curve). At the same pulling rate of  $\dot{\epsilon} = 1s^{-1}$ , the sample ( $n_{sc} = 18$ ,  $n_g = 4$ , and  $n_x = 149$ ) with  $\tau_R = 0.8$  s undergoes elastic debonding ( $\tau_R\dot{\epsilon} < 1$ ) without a tack peak followed by an increase in stress due to higher firmness ( $\beta = 0.37$ ) (black curve). The sample ( $n_{sc} = 18$ ,  $n_g = 8$ , and  $n_x = 450$ ) with characteristics ( $\beta = 0.24$ ,  $\tau_R = 2.5$  s) shows an intermediary behavior with a smaller tack peak and a slight increase in stress with deformation (blue curve).

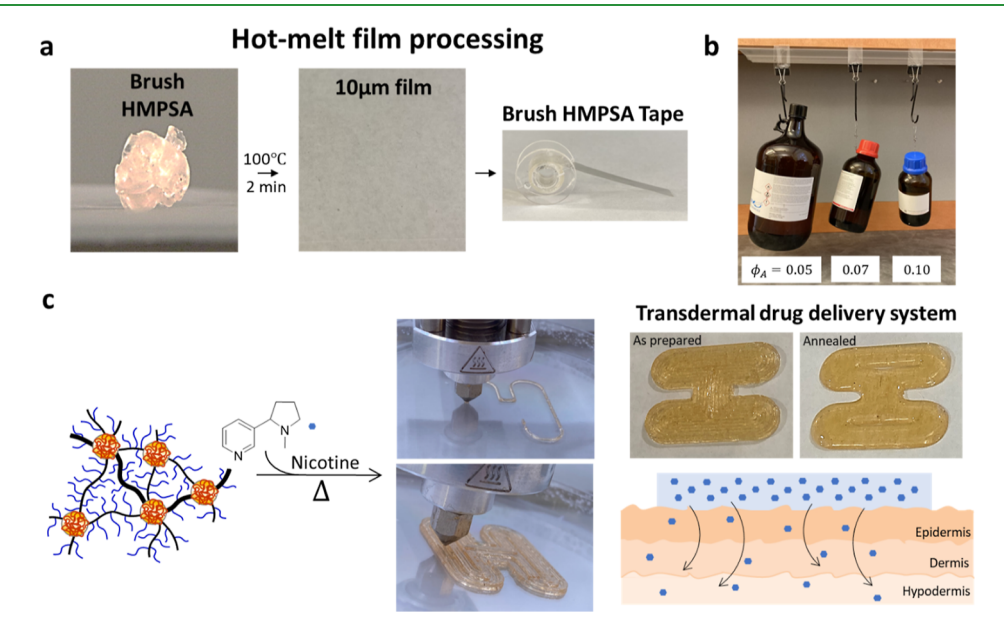


Figure 6. Moldability at moderate temperatures empowers thermal processing to manufacture additive-free brush HMPSA tapes and biomedical adhesives. (a) Manufacturing of brush HMPSA tapes. Brush HMPSAs samples with  $n_{\rm sc}=18$ ,  $n_{\rm g}=8$ ,  $n_{\rm A}=60$ ,  $n_{\rm bb}=1270$  and variable  $\phi_{\rm A}=0.05$ , 0.07, and 0.10 were pressed into to  $\sim 10~\mu$ m films at 100 °C on a cellulose backing, reducing the use of VOCs. The layered films were subsequently wound on a spool to manufacture tape rolls. (b) Zero-degree shear loads for brush HMPSA tapes with variable  $\phi_{\rm A}$ . The adhesive performance of the manufactured tapes dependent on architecture where the applied load (4–0.5 L solvent, left to right) appears to scale inversely in the  $\phi_{\rm A}$ . (c) Fused filament 3D-printing of a TDDS adhesive. The low viscosity of the brush HMPSAs at increased temperatures allows for mixing in active agents (nicotine) which diffuse into the skin of a patient when applied at room temperature. The TDDS may be processed via hot-melt press into a film backing or 3D-printing into unique shapes to aid in flexibility and mobility while applied to the patient.

## CONCLUSIONS

In conclusion, brush architecture unlocks unprecedented property control over viscoelastic and adhesive properties for a wide range of applications without the use of chemical additives. Specifically, the A-g-B architecture empowers wide-ranging control of the network modulus, the Rouse time, and strainstiffening with deformation by varying a distinct set of architectural parameters including the side chain length, grafting density, and volume fraction of the A block. This compels unprecedented structural control of the adhesive performance

covering almost 4 orders of magnitude of the work of adhesion and 6 orders of magnitude of debonding rates, spanning both viscoelastic and elastic debonding mechanisms. The ability to enhance the strain-stiffening behavior at large deformations prevents cohesive rupture, which in combination with the lack of additives results in no residue on a substrate after debonding. The physical nature of A-g-B networks allows for hot-melt preparation and 3D-printing of these PSAs with complex shapes. The ability to independently control  $n_{\rm A}$  and  $\phi_{\rm A}$  allows for tuning the flow temperature,  $T_{\rm flow}$ , for molding at moderate temper-

atures. Utilizing brush architecture, new chemistries to improve properties, such as solvent and UV resistance, can be introduced into HMPSA networks that had been previously thought to be unworkable for adhesives.

#### ASSOCIATED CONTENT

## **Supporting Information**

The Supporting Information is available free of charge at https://pubs.acs.org/doi/10.1021/acsami.3c07821.

Network synthesis, mechanical testing, adhesive testing, AFM data analysis, and scattering data analysis (PDF)

#### AUTHOR INFORMATION

#### **Corresponding Authors**

Mohammad Vatankhah-Varnosfaderani – Department of Chemistry, University of North Carolina at Chapel Hill, Chapel Hill, North Carolina 27599, United States;

orcid.org/0000-0001-7636-9099; Email: mvatankhah3188@gmail.com

Sergei S. Sheiko — Department of Chemistry, University of North Carolina at Chapel Hill, Chapel Hill, North Carolina 27599, United States; oorcid.org/0000-0003-3672-1611; Email: sergei@email.unc.edu

#### **Authors**

Mitchell R. Maw — Department of Chemistry, University of North Carolina at Chapel Hill, Chapel Hill, North Carolina 27599, United States; Oorcid.org/0000-0002-1921-4266

Alexander K. Tanas — Department of Chemistry, University of North Carolina at Chapel Hill, Chapel Hill, North Carolina 27599, United States

Erfan Dashtimoghadam — Department of Chemistry, University of North Carolina at Chapel Hill, Chapel Hill, North Carolina 27599, United States; orcid.org/0000-0001-5607-7961

Evgeniia A. Nikitina – Lomonosov Moscow State University, 119991 Moscow, Russian Federation

Dimitri A. Ivanov — Lomonosov Moscow State University, 119991 Moscow, Russian Federation; Institut de Sciences des Matériaux de Mulhouse-IS2M, CNRS UMR 7361, F-68057 Mulhouse, France; Sirius University of Science and Technology, 354340 Sochi, Russian Federation; orcid.org/0000-0002-5905-2652

Andrey V. Dobrynin – Department of Chemistry, University of North Carolina at Chapel Hill, Chapel Hill, North Carolina 27599, United States; oorcid.org/0000-0002-6484-7409

Complete contact information is available at: https://pubs.acs.org/10.1021/acsami.3c07821

#### **Author Contributions**

M.M. synthesized and characterized brush HMPSA networks; A.K.T aided in material synthesis; M.M. performed AFM analysis; A.V.D. provided theoretical analysis of mechanical properties; E.A.N. and D.A.I. conducted X-ray studies and data analysis; M.V. developed the concept of bottlebrush elastomers, S.S.S. is the principal investigator and corresponding author; and M.M. and S.S.S were primary writers of the manuscript. All authors discussed the results and provided feedback on the manuscript.

#### Notes

The authors declare no competing financial interest.

### ACKNOWLEDGMENTS

The authors gratefully acknowledge funding from the National Science Foundation (DMR 1921835, 1921858, and 1921923, DMR 2049518, and DMR 2004048). E.A.N. and D.A.I. acknowledge the Russian Science Foundation (RSF grant 23-73-30005). The authors acknowledge perfect technical support from the personnel of the ID02 beamline of the ESRF in Grenoble (France).

#### REFERENCES

- (1) Taboada, G. M.; Yang, K.; Pereira, M. J. N.; Liu, S. S.; Hu, Y.; Karp, J. M.; Artzi, N.; Lee, Y. Overcoming the Translational Barriers of Tissue Adhesives. *Nat. Rev. Mater.* **2020**, *5*, 310–329.
- (2) Fry, A. The Post-it Note: an Intrapreneurial Success. SAM Adv. Manag. J. 1987, 52, 4-9.
- (3) Márquez, I.; Alarcia, F.; Velasco, J. I. Synthesis and Properties of Water-Based Acrylic Adhesives with a Variable Ratio of 2-Ethylhexyl Acrylate and n-Butyl Acrylate for Application in Glass Bottle Labels. *Polymers* **2020**, *12*, 428–441.
- (4) Ju, Y. H.; Lee, H. J.; Han, C. J.; Lee, C. R.; Kim, Y.; Kim, J. W. Pressure-Sensitive Adhesive with Controllable Adhesion for Fabrication of Ultrathin Soft Devices. *ACS Appl. Mater. Interfaces* **2020**, *12*, 40794–40801.
- (5) Mehaffey, K. About That Leaky Ostomy Pouch. *Medsurg Nurs*. **2020**, 29, 347–354.
- (6) Abbott, S. Adhesion Science: Principles and Practice; DEStech Publications Inc., 2015.
- (7) Benedek, I. Technology of Pressure Sensitive Adhesives; CRC Press, 2018.
- (8) Yarusso, D. Adhesion Science and Engineering: Surfaces, Chemistry, and Applications; Elsevier Science and Technology, 2002; Vol. 1, pp 499–533.
- (9) Creton, C. Pressure-Sensitive Adhesives: an Introductory Course. *MRS Bull.* **2003**, 28, 434–439.
- (10) Creton, C.; Roos, A.; Chiche, A. Effect of Diblock Content on the Adhesive and Deformation Properties of PSA's Based on Styrenic Block Copolymers. In *Adhesion: Current Research and Applications*; Wiley-VCH Verlag GmbH & Co. KGaA, 2006; pp 337–361.
- (11) Gibert, F. X.; Marin, G.; Derail, C.; Allal, A.; Lechat, J. Rheological Properties of Hot-Melt Pressure-Sensitive Adhesives Based on Styrene—Isoprene Copolymers. Part 1: A Rheological Model for [SIS-SI] Formulations. *J. Adhes.* **2003**, *79*, 825–852.
- (12) Dahlquist, C. A. Proceedings of the Nottingham Conference on Adhesion Part III; Maclaren and Sons, 1966; Chapter 5; p 134.
- (13) Brandrup, J.; Immergut, E. H.; Grulke, E. A. *Polymer Handbook*, 4th ed.; Wiley-Interscience, 1999.
- (14) Creton, C.; Leibler, L. How Does Tack Depend on Time of Contact and Contact Pressure? *J. Polym. Sci., Part B: Polym. Phys.* **1996**, 34, 545–554.
- (15) Gay, C.; Leibler, L. Theory of Tackiness. *Phys. Rev. Lett.* **1999**, 82, 936–939.
- (16) Feldstein, M. M.; Siegel, R. A. Molecular and Nanoscale Factors Governing Pressure-Sensitive Adhesion Strength of Viscoelastic Polymers. J. Polym. Sci., Part B: Polym. Phys. 2012, 50, 739–772.
- (17) Shull, K. R.; Creton, C. Deformation Behavior of Thin, Compliant Layers Under Tensile Loading Conditions. *J. Polym. Sci., Part B: Polym. Phys.* **2004**, 42, 4023–4043.
- (18) Crosby, A. J.; Shull, K. R. Adhesive Failure Analysis of Pressure-Sensitive Adhesives. *J. Polym. Sci., Part B: Polym. Phys.* **1999**, 37, 3455–3472.
- (19) Creton, C.; Hooker, J.; Shull, K. R. Bulk and Interfacial Contributions to the Debonding Mechanisms of Soft Adhesives: Extension to Large Strains. *Langmuir* **2001**, *17*, 4948–4954.
- (20) Lakrout, H.; Sergot, P.; Creton, C. Direct Observation of Cavitation and Fibrillation in a Probe Tack Experiment on Model Acrylic Pressure-Sensitive-Adhesives. *J. Adhes.* **1999**, *69*, 307–359.
- (21) Rubinstein, M.; Colby, R. H. Polymer Physics; Oxford, 2012.

- (22) Ilyin, S. O.; Kostyuk, A. V.; Ignatenko, V. Y.; Smirnova, N. M.; Alekseeva, O. A.; Petrukhina, N. N.; Antonov, S. V. The Effect of Tackifier on the Properties of Pressure-Sensitive Adhesives Based on Styrene—Butadiene—Styrene Rubber. *Russ. J. Appl. Chem.* **2018**, *91*, 1945—1956.
- (23) Hansen, D.; Eiler, J.; Hansen, K.; Thormann, E. Dynamics of Water Absorption in Polymer Skin Adhesives. *ACS Appl. Bio Mater.* **2020**, *3*, 8698–8704.
- (24) Földes, E. Study of the Effects Influencing Additive Migration in Polymers. *Angew. Makromol. Chem.* **1998**, 261–262, 65–76.
- (25) Singh, A. K.; Mehra, D. S.; Niyogi, U. K.; Singh, G. Skin Irritation Study due to Electron Beam Cured Polyurethane Based Pressure Sensitive Adhesive Tape in Oryctolagus Cuniculus. *Res. J. Chem. Sci.* **2014**, *4*, 54–59.
- (26) Yan, J. W.; Hu, C.; Tong, L. H.; Lei, Z. X.; Lin, Q.-B. Migration Test and Safety Assessment of Polyurethane Adhesives Used for Food-Contact Laminated Films. *Food Packag. Shelf Life* **2020**, 23, 100449.
- (27) Eiler, J.; Hansen, D.; Bingöl, B.; Hansen, K.; Thormann, E. How the Viscoelastic and Sweat-Absorbing Properties of Skin Adhesives Affect Their Performance During Perspiration. *ACS Appl. Polym. Mater.* **2020**, *2*, 5533–5541.
- (28) Akiyama, S.; Kobori, Y.; Sugisaki, A.; Koyama, T.; Akiba, I. Phase Behavior and Pressure Sensitive Adhesive Properties in Blends of Poly(styrene-b-isoprene-b-styrene) with Tackifier Resin. *Polymer* **2000**, *41*, 4021–4027.
- (29) Doi, T.; Takagi, H.; Shimizu, N.; Igarashi, N.; Sakurai, S. Effects of Solubility Difference of Tackifier to Respective Components of Block Copolymers on Microphase-Separated Structures in Coated Layers of Pressure-Sensitive Adhesive Prepared by Solution Coating Process. ACS Appl. Polym. Mater. 2020, 2, 4973—4984.
- (30) Fujita, M.; Takemura, A.; Ono, H.; Kajiyama, M.; Hayashi, S.; Mizumachi, H. Effects of Miscibility and Viscoelasticity on Shear Creep Resistance of Natural-Rubber-Based Pressure-Sensitive Adhesives. *J. Appl. Polym. Sci.* **2000**, *75*, 1535–1545.
- (31) Daniel, W. F. M.; Burdyńska, J.; Vatankhah-Varnoosfaderani, M.; Matyjaszewski, K.; Paturej, J.; Rubinstein, M.; Dobrynin, A. V.; Sheiko, S. S. Solvent-Free, Supersoft and Superelastic Bottlebrush Melts and Networks. *Nat. Mater.* **2016**, *15*, 183–189.
- (32) Pakula, T.; Zhang, Y.; Matyjaszewski, K.; Lee, H. i.; Boerner, H.; Qin, S.; Berry, G. C. Molecular Brushes as Super-soft elastomers. *Polymer* **2006**, 47, 7198–7206.
- (33) Maw, M.; Dashtimoghadam, E.; Keith, A. N.; Morgan, B. J.; Tanas, A. K.; Nikitina, E.; Ivanov, D. A.; Vatankhah-Varnosfaderani, M.; Dobrynin, A. V.; Sheiko, S. S. Sticky Architecture: Encoding Pressure Sensitive Adhesion in Polymer Networks. *ACS Cent. Sci.* **2023**, *9*, 197–205.
- (34) Dobrynin, A. V.; Carrillo, J.-M. Y. Universality in Nonlinear Elasticity of Biological and Polymeric Networks and Gels. *Macromolecules* **2011**, *44*, 140–146.
- (35) Dashtimoghadam, E.; Maw, M.; Keith, A. N.; Vashahi, F.; Kempkes, V.; Gordievskaya, Y. D.; Kramarenko, E. Y.; Bersenev, E. A.; Nikitina, E. A.; Ivanov, D. A.; et al. Super-Soft, Firm and Strong Elastomers Toward Replication of Tissue Viscoelastic Response. *Mater. Horiz.* **2022**, *9*, 3022–3030.
- (36) Clair, C.; Lallam, A.; Rosenthal, M.; Sztucki, M.; Vatankhah-Varnosfaderani, M.; Keith, A. N.; Cong, Y.; Liang, H.; Dobrynin, A. V.; Sheiko, S. S.; et al. Strained Bottlebrushes in Super-Soft Physical Networks. *ACS Macro Lett.* **2019**, *8*, 530–534.
- (37) Varkey, J. T.; Augustine, S.; Thomas, S. Thermal Degradation of Natural Rubber/Styrene Butadiene Rubber Latex Blends by Thermogravimetric Method. *Polym.-Plast. Technol. Eng.* **2000**, 39, 415–435.
- (38) Adams, J. L.; Graessley, W. W.; Register, R. A. Rheology and the Microphase Separation Transition in Styrene-Isoprene Block Copolymers. *Macromolecules* **1994**, 27, 6026–6032.
- (39) Toporowski, P. M.; Roovers, J. E. L. Glass Transition Temperature of Low Molecular Weight Styrene–Isoprene Block Copolymers. J. Polym. Sci., Polym. Chem. Ed. 1976, 14, 2233–2242.

- (40) Han, C. D.; Baek, D. M.; Kim, J. K. Effect of Microdomain Structure on the Order-Disorder Transition Temperature of Polystyrene-Block-Polyisoprene-Block-Polystyrene Copolymers. *Macromolecules* **1990**, 23, 561–570.
- (41) Gent, A. N.; Wang, C. Fracture Mechanics and Cavitation in Rubber-Like Solids. *J. Mater. Sci.* **1991**, *26*, 3392–3395.
- (42) Zhalmuratova, D.; La, T. G.; Yu, K. T. T.; Szojka, A. R. A.; Andrews, S. H. J.; Adesida, A. B.; Kim, C. i.; Nobes, D. S.; Freed, D. H.; Chung, H. J. Mimicking "J-Shaped" and Anisotropic Stress—Strain Behavior of Human and Porcine Aorta by Fabric-Reinforced Elastomer Composites. *ACS Appl. Mater. Interfaces* **2019**, *11*, 33323—33335.